

Kinematics of the molecular interstellar medium probed by Gaia: steep velocity dispersion-size relation, isotropic turbulence, and location-dependent energy dissipation

Ji-Xuan Zhou,¹ Guang-Xing Li,¹★ Bing-Qiu Chen,¹†

¹ South-Western Institute for Astronomy Research, Yunnan University, Chengong District, Kunming 650091, P. R. China

31 March 2022

ABSTRACT

The evolution of the molecular interstellar medium is controlled by processes such as turbulence, gravity, stellar feedback, and Galactic shear. As a part of the **ISM-6D** project, using Gaia astrometric measurements towards a sample of young stellar objects (YSOs), we study the morphology and kinematic structure of the associated molecular gas. We identify 150 YSO associations with distance $d \lesssim 3$ kpc. The YSO associations are elongated, with a median aspect ratio of 1.97, and are oriented parallel to the disk midplane, with a median angle of 30° . The turbulence in the molecular clouds as probed by the YSOs is isotropic, and the velocity dispersions are related to the sizes by $\sigma_{v,2D} = 0.74 (r/\text{pc})^{0.67}$ (km/s). The slope is on the steeper side, yet consistent with previous measurements. The energy dissipation rate of turbulence $\dot{\epsilon} = \sigma_{v,3D}^3/L$ decreases with the Galactocentric distance, with a gradient of 0.2 dex kpc^{-1} , which can be explained if turbulence is driven by cloud collisions. In this scenario, the clouds located in the inner Galaxy have higher chances to accrete smaller clouds and are more turbulent. Although the density structures of the complexes are anisotropic, the turbulence is consistent with being isotropic. If the alignment between density structures and the Galactic-disk mid-plane is due to shear, we expect $t_{\text{cloud}} \gtrsim t_{\text{shear}} \approx 30$ Myr. This cloud lifetime is longer than the turbulence crossing time, and a continuous energy injection is required to maintain the turbulence.

Key words: Galaxies: ISM – ISM: structure – ISM: kinematics and dynamics – Stars: formation – Physical data and processes: turbulence

1 INTRODUCTION

The collapse of molecular clouds is a complex processes characterized by interplays between e.g. gravity, turbulence (Larson 1981) and magnetic field (Li et al. 2014). The clouds exhibit complex density and velocity structures. Larson (1981) found the velocity dispersion σ_v of a cloud is positively correlated with its size l by $\sigma_v \sim l^\beta$ where $\beta = 0.38$. The slope can be explained by the cascade of Kolmogorov-like turbulence (Kolmogorov 1941). This relation is called the Larson relation, and the role of turbulence in star formation is well-recognized ever since. However, the slope of the Larson relation remains uncertain, and the interpretation of turbulence cascade has been challenged. Solomon et al. (1987) found that the velocity dispersion σ_v of a cloud is related to its size l by $\sigma_v \sim l^{0.5}$ from 273 molecular clouds observed by the Five College Radio Astronomy Observatory (FCRAO), where the scaling exponent is larger than 0.38 as found by Larson (1981). Similar results are also reported in e.g. Bolatto et al. (2008). Heyer et al. (2009); Ballesteros-Paredes et al. (2011) proposed that the slope of the Larson relation can also be explained assuming self-gravity. Recently, Izquierdo et al. (2021) simulated the evolution of molecular clouds in galaxy discs, and found that the exponent varies from 0.3 to 1.2.

The fact that larger velocity dispersions are found at larger scales

suggests that the kinetic energy of molecular clouds is injected from the outside. To constrain turbulence injection, a promising direction is to identify coherent gas structures. Li et al. (2013) identified a kpc-sized coherent structure called the “500 pc filamentary gas wisps”, and Goodman et al. (2014) discovered an object called “extended Nessie” of a similar size. These discoveries suggest that the molecular clouds are not separated objects but an inseparable part of the Milky Way interstellar medium. Subsequent works studied samples of such filaments (Ragan et al. 2014; Abreu-Vicente et al. 2016; Wang et al. 2015; Li et al. 2016). Li et al. (2016) extracted filamentary structures from the APEX Telescope Large Area Survey of the Galaxy (ATLASGAL, Schuller et al. 2009) survey. They found that the filamentary structures tend to stay parallel to the Galactic disk mid-plane, indicating that Galactic shear plays an important role in shaping the structures of the molecular interstellar medium. Another possible consequence of shear is that it can lead to velocity anisotropy, e.g. the velocity dispersion of molecular clouds measured along the Galactic longitude l direction is larger compared to that along the Galactic latitude b direction. Koda et al. (2006) attempted to constrain the importance of shear by studying the radial velocity structures of the Boston University–Five College Radio Astronomy Observatory Galactic Ring Survey (GRS) clouds (Jackson et al. 2006), and found that the velocity gradient has no preferred direction. Whether the velocity field is isotropic or anisotropic remains unclear.

We study the properties and Galactic distribution of a sample of

★ gxli@ynu.edu.cn

† bchen@ynu.edu.cn

YSO associations using Gaia data. YSOs are stars at the very early stage of stellar evolution and are usually close to where they were born, such that they inherit the velocity of gas from which they originate and their locations may indicate the shape of molecular clouds. [Großschedl et al. \(2021\)](#); [Lim et al. \(2021\)](#) compared the velocities of YSOs against the velocity of the ambient molecular gas, and found a good agreement. This technique has already been used in previous studies to study e.g. turbulent motion of molecular gas ([Ha et al. 2021](#)). [Li & Chen \(2021 under review\)](#) used a similar approach to study the velocity structure of a Galactic filament called the Gould Belt Radcliffe Wave ([Alves et al. 2020](#)). In this paper, most YSO associations have sizes similar to that of the clouds, in most cases, they are associated with molecular clouds ([Zhou, Li et al in prep](#)). The Gaia survey ([Gaia Collaboration et al. 2016](#)) provides accurate measurements of the magnitudes, parallaxes, and proper motions of stars in the Milky Way. We use the Gaia Data Release 2 (DR2, [Gaia Collaboration et al. 2018](#)) measurements of young stellar objects to study the kinematics of the gas they associate with. Using a sample of 15149 YSOs which are younger than 3 Myr and located from -6 to -10 kpc from the Galactic center, we identify a sample of ~ 100 molecular cloud-sized YSO associations and study the kinematics of the molecular interstellar medium from several pc to one hundred pc scale.

2 DATA & METHOD

2.1 YSO data

Our YSO sample, which consists of 15149 Class I and Class II YSOs, is selected from [Marton et al. \(2016\)](#). [Marton et al. \(2016\)](#) obtained those YSOs by applying the Support Vector Machine method to a combined dataset containing the AllWISE catalog of the Wide-field Infrared Survey Explorer ([Cutri et al. 2021](#)), the Two Micron All-Sky Survey (2MASS [Cutri et al. 2003](#)), and the Planck dust opacity values ([Planck Collaboration et al. 2014](#)). Their parallaxes and proper motions are derived by crossing-matching with Gaia DR2 ([Gaia Collaboration et al. 2018](#)). According to [Dunham et al. \(2015\)](#), age for Class I YSO is about 0.78 Myr and age for Class II YSO is 2 or 3 Myr. As the timescale is shorter than the crossing time of molecular cloud turbulence, we expect them to inherit the positions and velocities of the gas they originate from ([Li & Chen 2021 under review](#)). We further remove YSOs whose parallax errors are larger than 20%.

2.2 Estimating the spatial density

We use the python function `hist3d` to produce a YSO density map in l , b , and $\log(d)$ space, where d : the distance to the Sun. Our density map has $0^\circ < l < 360^\circ$, $-25^\circ < b < 25^\circ$, $3.5 \text{ pc} < d < 7300 \text{ pc}$. We divide l into 720 bins separated by 0.5° , b into 100 bins separated by 0.5° and $\log(d)$ into 50 bins. The density map is smoothed with a Gaussian filter with $\sigma = 0.6$ pixel. The results are plotted in Fig. 1.

2.3 Identifying structures

We use the Dendrogram program ([Rosolowsky et al. 2008](#)) to extract structures from the YSO density map. Dendrogram is a program to extract structures from maps by exploiting the topological relation between isosurfaces. The results are dependent on three parameters: `min_value`, `min_delta`, and `min_npix`, where `min_value` means

the minimum value to be considered as a structure, `min_delta` refers to the value difference between structures and substructures, and `min_npix` is the smallest number of pixels contained in one structure.

Through experiments, we set `min_value` = 0.1, `min_delta` = 0.3, and `min_npix` = 10, and obtain a total of 518 structures, which contain 10 to 2593 pixels. One pixel might belong to a few nested structures. All structures found by Dendrogram are called “associations”. Some of the small associations are part of the larger ones, and a few examples are shown in Fig. 2. Each YSO can belong to one or a few associations, and their memberships are determined by matching their locations to the footprints of identified structures. We further remove associations that contain very few stars (≤ 15), and obtain a sample of 219 associations which are coherent in space and contain reasonable numbers of stars.

2.4 Identifying member YSOs

Almost all YSO associations contain significant amounts of contaminants, as reflected from their distance distributions. To address this, we apply a Gaussian Mixture Model (`sklearn.mixture`) to the distance distributions. The component number is allowed to vary from 1 to 4, after which the best-fitting one is selected based on the Akaike Information Criterion (AIC), which describes the simplicity and precision of the model. This procedure leaves us with a number of Gaussian components named $G(d_i, \text{Ed}_i)$, where d_i is the mean distance and Ed_i is the distance dispersion. We first select the most dominant components as $G(d_p, \text{Ed}_p)$. If there is an additional component staying close to the most dominant one ($|d_i - d_p| < 1.6 \text{Ed}_p$), they will be merged together, after which a valid distance range is determined as where $\text{PDF}_{\text{merged}}(d) > 0.1 \text{PDF}_{\text{total}}(d)$, as indicated in Fig. 3, where PDF stands for the probability density distributions. A YSO is a member of the association if its distance is within the range as determined by this procedure. If a significant fraction ($\geq 65\%$) of the member YSOs do not belong to the merged component, the association is removed from the sample. An example illustrating this procedure is plotted in Fig. 3.

2.5 Final sample

After removing the contaminations in associations, we apply the following criteria to obtain a sample of YSO associations whose physical properties can be estimated reliably: (1) the number of stars is more than 20, and (2) the dispersion of distance is smaller than 0.35 kpc. Finally, we obtain a sample of 150 YSO associations, which are described in Appendix A.

The member stars have spatial distributions that resemble the molecular gas they originate from, and in the majority of the cases, their velocity distributions are Gaussian-like. One example is presented in Fig. 4, which corresponds to the well-known Orion molecular clouds. Here, we plot the distributions of member stars in the $l - b$ and $v_l - v_b$ space. In the $l - b$ space, the YSO association resembles the Orion molecular cloud, and in the velocity space, the YSOs are clustered.

2.6 Deriving physical properties

For each YSO association, we derive the following properties.

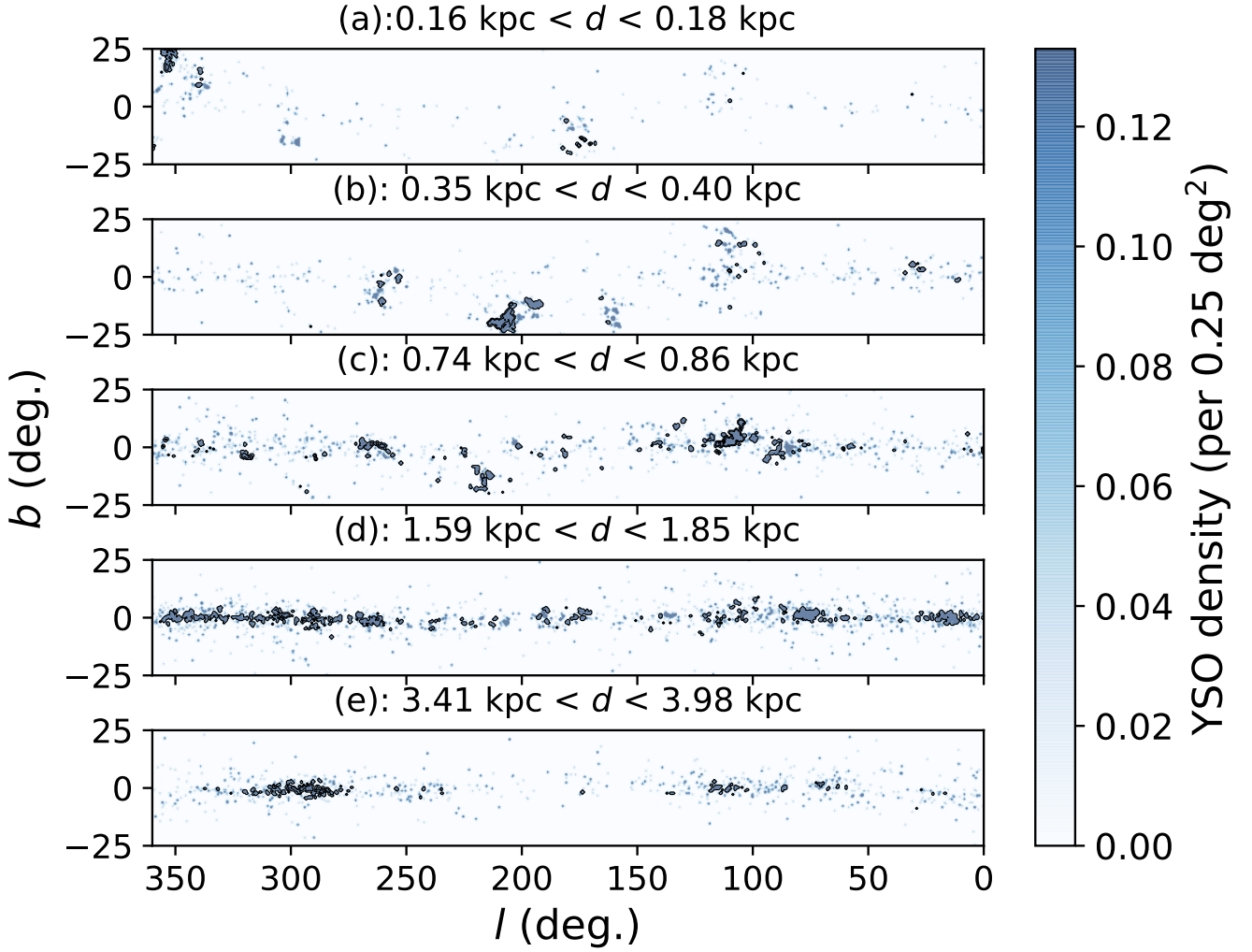


Figure 1. Spatial density of the YSO sample at five distance channels. The colors represent the YSO density, and the black contours represent the boundaries of the associations found by Dendrogram.

2.6.1 Distance and velocity dispersion

We use the Random Sample Analysis to estimate the distance and velocity uncertainties. For each proper motion and distance measurements, assuming the errors follow a Gaussian distribution, we generate a number of realizations according to the measured uncertainties in parallax and proper motion, from which distances and proper motions as well as the statistical uncertainties can be derived.

In practice, the measured parameters include the proper motions and parallaxes of its member stars. We start by generating $N = 1000$ new measurements where we added uncertainties to the parameters according to the expected random measurement errors. To measure the distance and its uncertainty, assuming the mean distances of a realization is $d_{\text{mean},i}$, the mean distance is $\text{mean}(d_{\text{mean},i})$, and the uncertainty of distance estimate is $\text{std}(d_{\text{mean},i})$, where std stands for the standard deviation. Similar approaches can be used to measure the velocity dispersion and its uncertainty.

(Using the proper motion uncertainty and distance uncertainty, we generate 1000 new measurements for each stars' velocity in l and b directions and 2D velocity. Assuming the mean velocity of one ve-

locity distribution in the 1000 realizations is $v_{\text{mean},i}$ and the standard deviation of the velocity distribution is $\sigma_{v,i}$, the mean velocity for an association is $\text{mean}(v_{\text{mean},i})$, velocity dispersion σ_v is $\text{mean}(\sigma_{v,i})$, and velocity dispersion error $E(\sigma_v)$ is $\text{std}(\sigma_{v,i})$.)

2.6.2 Size

The dataset allows us to study the motion along l and b directions separately. To fully exploit this potential, we derive three sizes: size in l direction - r_l , size in b direction - r_b , and overall size r . These are full width at half maxima (FWHM) widths, e.g. $r_l = 2.355 d \cdot \text{std}(l_i)$, and $r_b = 2.355 d \cdot \text{std}(b_i)$, where l_i , b_i are positions of the member YSOs in one association. The size r is estimated using: $r = 2.355 d \cdot \sqrt{(\sigma_{\min}^2 + \sigma_{\max}^2)/2}$, where $r_{\min} = \sigma_{\min} d$ and $r_{\max} = \sigma_{\max} d$, and σ_{\min} , σ_{\max} are the dispersions measured along the major and minor axes of the spatial distributions on sky, and are the parameters we derive from the fitting ellipses in Sec. 2.6.3. d is the mean distance of every association. Our associations have sizes ranging from several pc to hundreds of pc. The intrinsic width of the cloud is estimated as

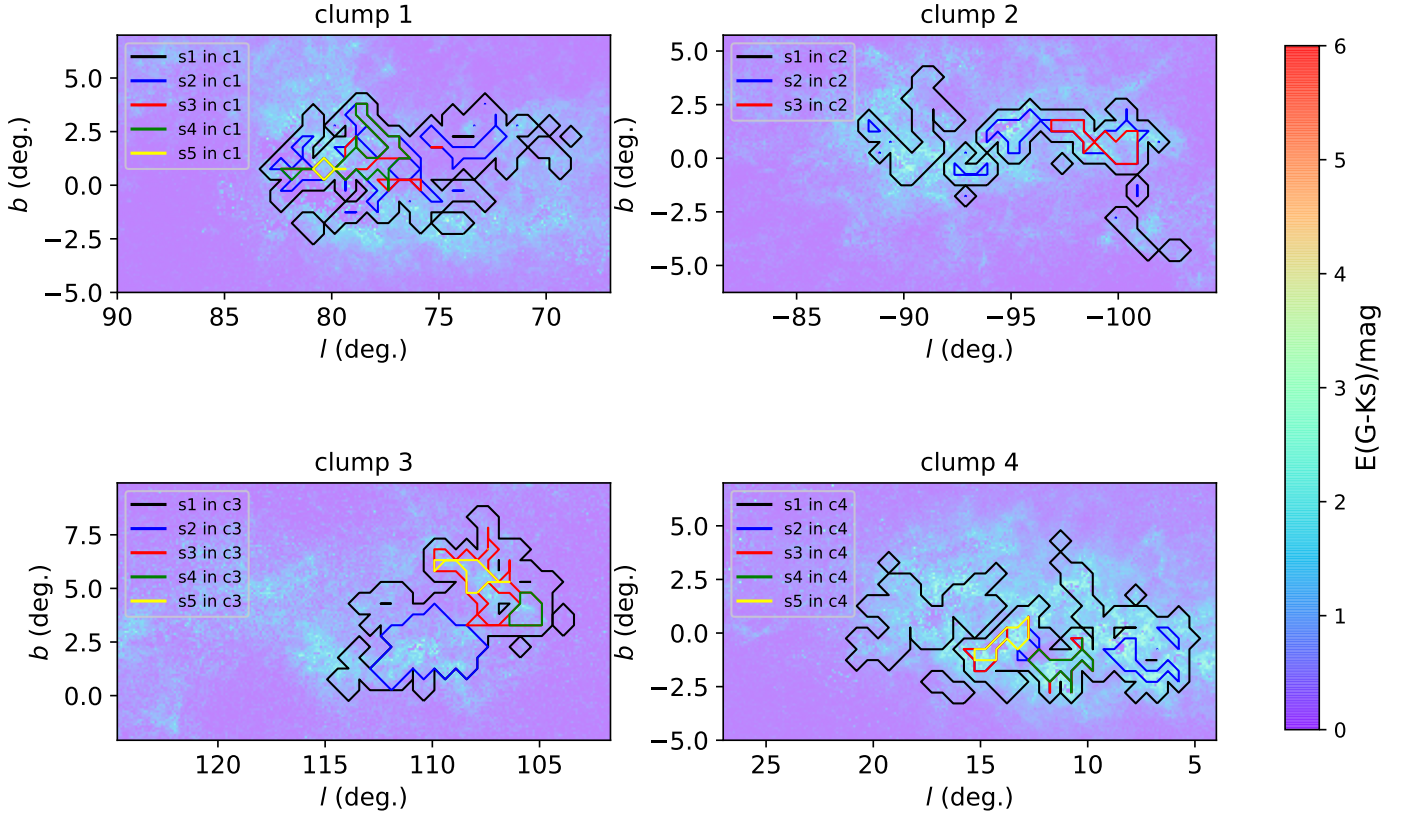


Figure 2. Examples of nested structures. The background is the 2D dust map from [Chen et al. \(2019a\)](#) integrated from $d = d_{\text{mean}} - \delta_d$ to $d = d_{\text{mean}} + \delta_d$, where d_{mean} is the mean distance, and δ_d is the widths. Contours represent boundaries of the associations.

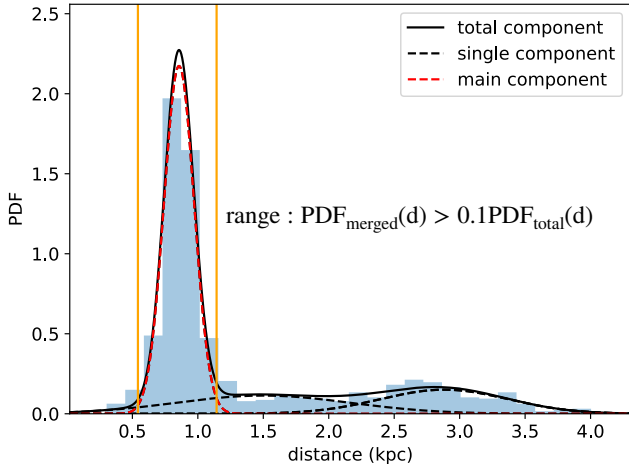


Figure 3. Generate a clean sample of member YSOs. The histogram represents the distance distribution of YSOs that belongs to one of our complexes. The solid black line refers to the overall best-fitting distribution selected from a range of models based on the AIC, and the dashed lines represent different Gaussian components. These are derived using `sklearn.mixture`. The red dashed line is the dominant merged component, and the two vertical orange lines mark the final distance range. YSOs that stay within this distance range will be considered in our analyses.

width = $\sqrt{\text{std}(d_i)^2 - \text{std}(d_{\text{err}_i})^2}$ where d_i is the distance of object i and the corresponding error is d_{err_i} .

2.6.3 Aspect ratios and Orientations

For each association, we fit ellipses to the distribution of member YSOs in the spatial ($l-b$) and velocity (v_l-v_b) space by diagnosing a tensor constructed from the spatial and velocity dispersions (e.g. the tensor is $T_{i,j} = \sum p_i, p_j$, where p is the spatial/velocity coordinates, and i, j represent l, b directions), from which the lengths of the major and minor axes $\sigma_{\text{max}}, \sigma_{\text{min}}$ as well as their orientations can be determined. These allow us to measure the orientation of the object from this major axes as well as the aspect ratios. Spatially, we measure the position angle PA_{l-b} and the aspect ratio A_{l-b} and in the velocity space, we also measure the position angle $\text{PA}_{v_l-v_b}$ and the aspect ratio $A_{v_l-v_b}$.

3 RESULTS

3.1 Galactic distribution and size

In Fig. 5 we plot locations of the associations in the Milky Way disk, where a map of the distribution of dust from [Chen et al. \(2019a\)](#) is overlaid. The complexes are associated with dust and are organized along a few filaments. This is expected, as the YSOs are young and are associated with the molecular cloud which contains dust. In Fig.

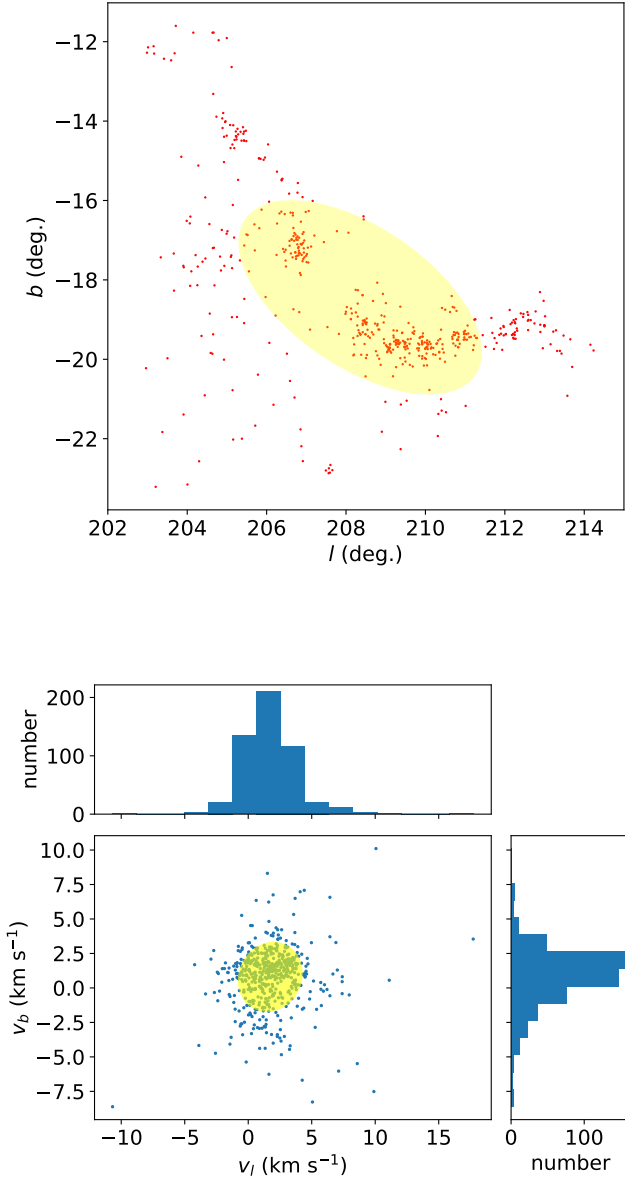


Figure 4. Locations of the member YSOs of one of our associations in the $l-b$ and v_l-v_b space. **Upper panel:** Locations in the $l-b$ plane. Red dots are the member stars of this structure and the yellow ellipse represents the fitting result, as described in section 2.6.3, through which the aspect ratio and the orientation are measured. **Lower panel:** Locations of member YSOs in the v_l-v_b space. The yellow ellipse represents the fitting result, where the heights of the ellipses are $2 r_{\min}$.

5, we plot the distribution of the number of member stars contained in the complexes, as well the size distribution. The associations have sizes that range from 10 to 100 pc, which is similar to the sizes of molecular clouds obtained by e.g. Roman-Duval et al. (2010) and Chen et al. (2020).

3.2 Aspect ratio and Orientation

Our YSO associations are angled mostly parallel to the disk mid-plane. To illustrate this, we plot the distributions of the position angle and aspect ratio of the ellipses respecting the distributions of member YSOs in the $l-b$ and the v_l-v_b space (Fig. 6). In the $l-b$ space, the associations appear to be elongated, with a median aspect ratio of 1.97, and they tend to stay aligned with the Galactic disk mid-plane, with a median angle of 30° with respect to the mid-plane. In the v_l-v_b space, the distribution has a median aspect ratio of 1.82 and a median angle of 27.7° , where the velocity dispersion is larger along the Galactic longitude. The difference between the position angle measured in space and the velocity space is also small, with a median angle difference of 24.33° .

3.3 Velocity-Size Relation, and Velocity Anisotropy

We study the relation between velocity dispersion and size using our YSO associations. This relation was proposed by Larson (1981) and is called the Larson relation. In previous studies, the velocity dispersions are estimated using the spectral lines from molecules such as the CO, along the radial direction. We present a first study of the Larson relation using the Gaia proper motions. This allows us to study the relation between separation and velocity dispersion measured along l and b directions separately.

Our result is plotted in Fig. 7. Along l ,

$$\sigma_{v_l} = 0.58 (r_l/\text{pc})^{0.66} \text{ (km/s)}, \quad (1)$$

and along b ,

$$\sigma_{v_b} = 0.54 (r_b/\text{pc})^{0.64} \text{ (km/s)}. \quad (2)$$

and combining together using $\sigma_{v,2D} = (\sigma_{v_{\min}}^2 + \sigma_{v_{\max}}^2)^{1/2}$, where $\sigma_{v_{\max}}$ and $\sigma_{v_{\min}}$ are the dispersions measured along the longer and shorter axes of the velocity dispersion ellipse, thus

$$\sigma_{v,2D} = 0.74 (r/\text{pc})^{0.67} \text{ (km/s)}. \quad (3)$$

Our first finding is that the velocity dispersions measured along the l and b directions are almost identical, which means that although the density structure of the region is anisotropic along z direction and in the xy plane, the turbulence is isotropic. To verify this, we plot the ratio between the projected length along the Galactic longitude and latitude direction r_l/r_b again the size r , and as well as the velocity dispersion ratio $\sigma_{v_l}/\sigma_{v_b}$ against the size r and find the following relation:

$$r_l/r_b \propto (r/\text{pc})^{0.22},$$

Assuming a Larson relation of $\sigma_v \propto r^{0.67}$, we have

$$\sigma_{v_l}/\sigma_{v_b} \propto (r_l/r_b)^{0.22 \times 0.67} \propto (r/\text{pc})^{0.15},$$

which is consistent with our fitting results: $\sigma_{v_l}/\sigma_{v_b} \propto r^{0.14 \pm 0.04}$. All the relations in Fig. 7 are consistent with the turbulence being isotropic.

The scaling exponent 0.67 is steeper than 0.38 in Larson (1981) but close to recent results (e.g. Shetty et al. 2012; Hughes et al. 2013; Kauffmann et al. 2017; Sun et al. 2018; Liu et al. 2021). The slope can be explained if the turbulence is compressible (Kritsuk et al. 2013; Cen 2021), or if the turbulence is driven by accretion and gravitational contraction (e.g. Dobbs et al. 2011; Ibáñez-Mejía et al. 2016a; Izquierdo et al. 2021).

We also considered the crossing time for the clouds, which is

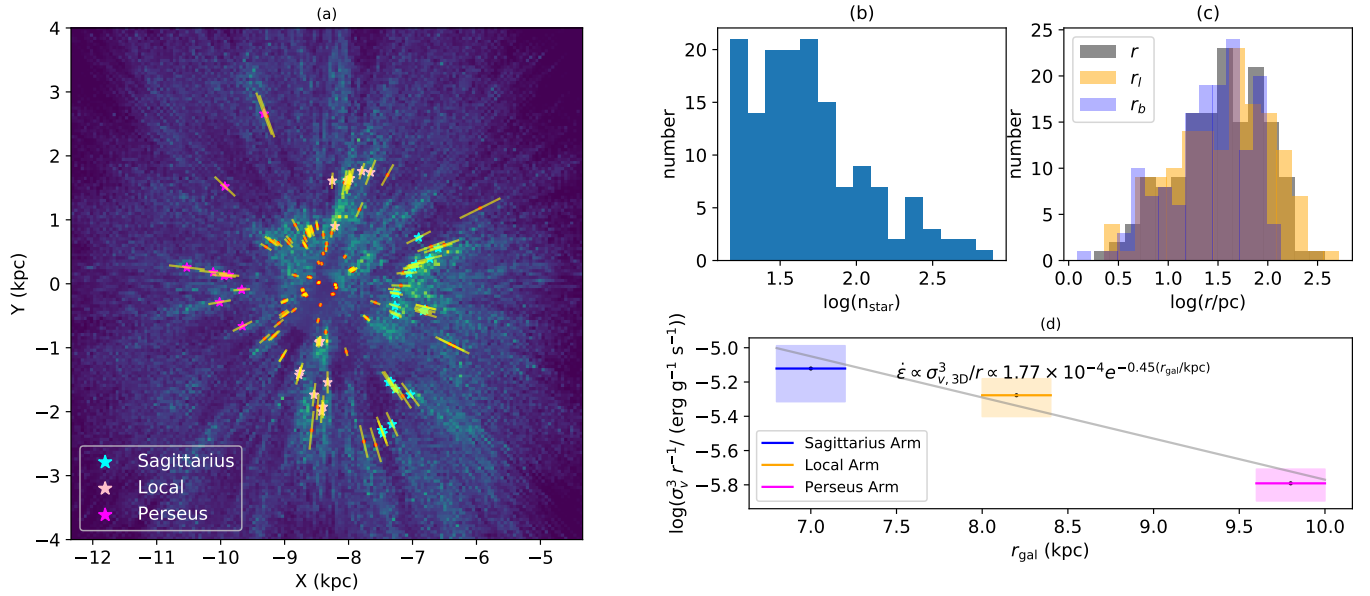


Figure 5. Properties, Galactic distribution, and energy dissipation rate of YSO associations. **Panel (a):** Location of the associations on the X-Y plane. The sun locates at $(-8.34, 0)$ and the center of the Milky Way locates at $(0, 0)$. Red dots represent the locations of 150 associations and yellow lines show their distance uncertainties. The background dust map is from [Chen et al. \(2019a\)](#). The cyan, pink, and fuchsia stars refer to the associations located on the Sagittarius Arm, the Local Arm, and the Perseus Arm respectively, and the bars represent distance uncertainties. **Panel (b):** Histogram of the number of member stars for all 150 associations. **Panel (c):** Histogram of the size of associations. The Grey one represents the distribution of the overall size, the yellow one represents the sizes measured along the Galactic longitude (l) direction, and the purple one represents the sizes measured along the Galactic latitude (b) direction. **Panel (d):** Energy dissipation rate for three spiral Arms. Fuchsia, orange and blue lines with error bars present the energy dissipation rate of associations located on the Perseus Arm, the Local Arm, and the Sagittarius Arm respectively, where the corresponding errors are also indicated using the extents of the boxes. The grey line is the fitting result where $\dot{\epsilon} = 1.77 \times 10^{-4} e^{-0.45(r_{\text{gal}}/\text{kpc})}$ (erg g⁻¹ s⁻¹).

determined using: $t_{\text{cross}} = 2R/\sigma_v$, where R is the radius of the cloud and σ_v is the 2D velocity dispersion. We plotted the lines representing different crossing times in the upper left panel in Fig. 7. The red line is the shear time we derived from the Oort constant: $A = 16.31 \pm 0.89$ km s⁻¹ kpc⁻¹ ([Wang et al. 2021](#)), which can describe the shearing caused by the Galactic rotation in the Solar neighborhood ([Oort 1927](#); [Kerr & Lynden-Bell 1986](#)). All our associations have crossing time much shorter than 30 Myr, implying that the importance of shear is insignificant compared to that of the turbulence.

3.4 Energy dissipation rate in different spiral Arms

In the Kolmogorov theory of turbulence, energy injected into turbulence on large scales will dissipate on small scales. Following [Mac Low \(1999\)](#), we parameterize the turbulent energy dissipation rate as $\dot{\epsilon}_{\text{kin}} = \eta k \sigma_v^3$, where σ_v refers to the velocity dispersion of the cloud scale, and k is the driving wavenumber ($k \approx 1/r$). So $\dot{\epsilon} = \sigma_v^3/r$ describes the energy dissipation of molecular cloud turbulence, and here we investigate its variations with respect to their locations in the Galactic disk.

Following previous papers ([Chen et al. 2019b](#)), we separate the clouds into groups associated with different spiral arms (the Sagittarius, Local and Perseus Arm, see Fig. 5), and study the energy dissipation rate measured in terms of $\dot{\epsilon}$. Since it is hard to resolve small clouds at large distances, for each group, we select median-sized associations ($40 < r < 130$ pc), and estimate the energy dissipation rate using $\dot{\epsilon} = \sigma_{v,3D}^3/r$. $\sigma_{v,3D}$ is the 3D velocity dispersion estimated using: $\sigma_{v,3D} = \sqrt{3/2}\sigma_{v,2D}$. Our results are plotted in the lower right panel of Fig. 5. We note that here we are deriving an

un-normalized version of the energy dissipation rate, as the “true” energy dissipation rate is still dependent on a normalizing factor ([Frisch 1995](#), as summarized by [Qian et al. 2018](#)), as well as the efficiency parameter η , which we can not constrain directly. We find that the energy dissipation rate decreases with increasing distance from the Galactic center. By fitting it using an exponential model we find $\dot{\epsilon} = 1.77 \times 10^{-4} e^{-0.45(r_{\text{gal}}/\text{kpc})}$ (erg g⁻¹ s⁻¹) where r_{gal} is the Galactocentric distance, which implies a gradient of 0.20 dex kpc⁻¹.

4 DISCUSSIONS

4.1 Stationary, anisotropic density structures supported isotropic turbulence

The fact that the associations tend to stay aligned with the disk mid-plane given an isotropic turbulence despite anisotropic density structures is somewhat surprising. This is because the very process which leads to the alignment of associations should also leave some imprints on the velocity. One explanation is that the associations are long-lived entities, with their lifetime as long as the shear time, such that shear can stretch the clouds horizontally, aligning the gas associated with the YSOs associated to the Galactic disk.

The clouds are thus likely to be objects with $t_{\text{crossing}} < t_{\text{cloud}} \approx t_{\text{shear}}$, such that shear have sufficient time to align the gas. During the cloud lifetime, turbulence is maintained by a continuous injection. In the Solar neighborhood, assuming a Oort constant of $A \approx 16$ km s⁻¹ kpc⁻¹ ([Wang et al. 2021](#)), we expect a cloud lifetime of $t_{\text{cloud}} \gtrsim t_{\text{shear}} = \kappa^{-1} = (1/r)|d\Omega/dr| = (2A)^{-1} = 30$ Myr where κ is the shear rate. This is longer than the crossing time of some of

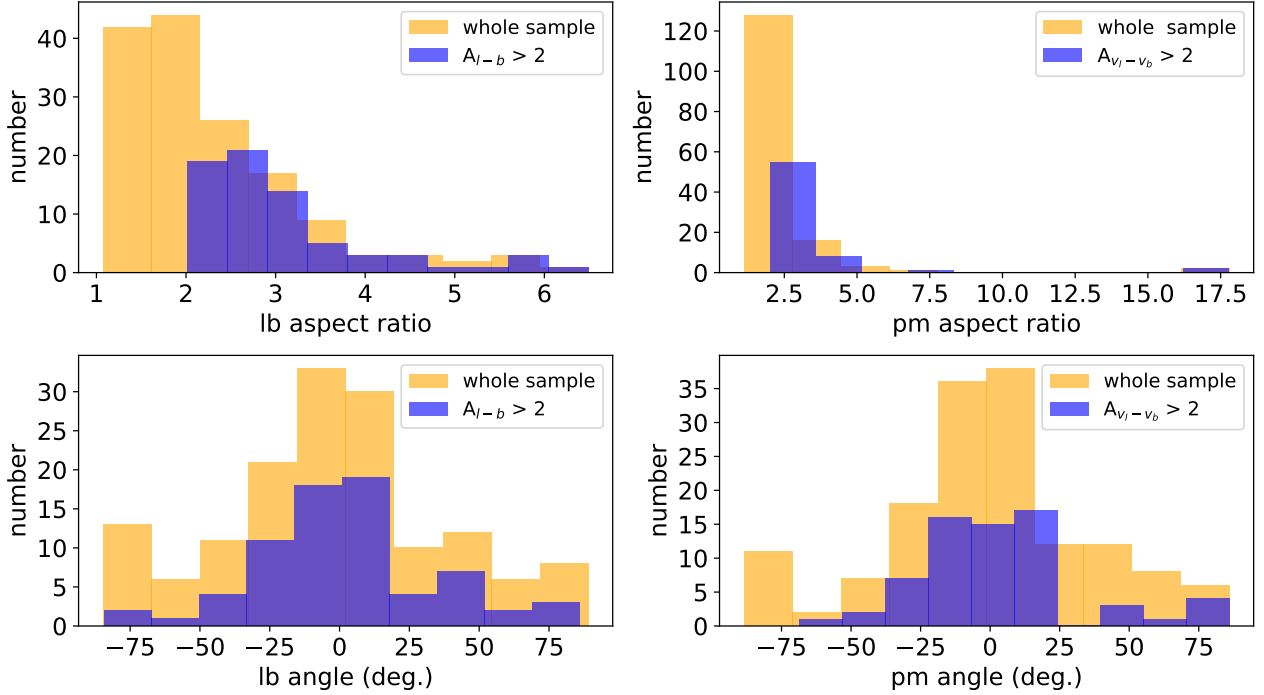


Figure 6. Distributions of position angles and aspect ratios measured in the $l-b$ and v_l-v_b space. **Upper left:** Distribution of aspect ratio in $l-b$ space. **Lower left:** Distribution of the position angle in $l-b$ space. **Upper right:** Distribution of aspect ratio in v_l-v_b space. **Lower right:** Distribution of the position angle in v_l-v_b space. The Orange histograms represent the distribution of the whole 150 structures, the purple histograms represent those with aspect ratios greater than 2 in the four figures.

the largest association in our sample, where $t_{\text{cross}} \approx 20$ Myr. This is comparable to results inferred from the evolution of cloud population evolutions (Meidt et al. 2015; Koda 2021), but is shorter than the lifetime derived by comparing the locations of H II regions with the locations of clouds (Kruijssen et al. 2019).

These results also provide insights into the nature of turbulence in clouds. There are different schools of thought concerning the link between density and velocity structures. The first believes that turbulence creates the density structure upon which collapse occurs (Vázquez-Semadeni et al. 2017). Padoan & Nordlund (2002) found the slope of the stellar (Initial Mass Function) IMF can be predicted and produced by the turbulence. The second believes that the role of turbulence is to provide support, where only gravitationally bound density fluctuations can collapse (Hennebelle & Chabrier 2008; Hopkins 2013). The third, particularly Mac Low (2003) believes that the role of supersonic turbulence is to provide support, leading to slower collapse and longer cloud lifetime. Our results favor the third one. The density structures appear to be supported by turbulence and long-lived.

4.2 Energy source of molecular clouds

Our results indicate that the energy dissipation rate of turbulence decreases with the Galactocentric distance. This can be explained if the turbulence is driven by molecular cloud coagulations. Along this line of thought, Klessen & Hennebelle (2010) and Elmegreen & Burkert (2010) argued that accretion can explain the observed level of turbulence at the Galactic, molecular cloud and core scales. Using an analytical model and numerical simulations, Dobbs et al. (2011), Goldbaum et al. (2015) and Ibáñez-Mejía et al. (2016b) demonstrated

that a large cloud can maintain its turbulence by accreting smaller clouds.

Our conclusion results from the fact that molecular clouds are more turbulent in gas-rich regions in the Milky Way disk as characterized by Σ_{disk} . This fact can be explained in the collision-driven turbulence scenario, where regions of higher densities have higher cloud-cloud collision rates, leading to more turbulence. Quantitatively, Li (2017) studied the co-evolution between the Galactic disk and molecular cloud, and proposed the following equation linking the properties of the disk to the energy dissipation rate of the molecular cloud:

$$\sigma_{v,\text{cloud}} \approx \sigma_{v,\text{disc}} \left(\frac{\Sigma_{\text{disc}}}{\Sigma_{\text{cloud}}} \right)^{1/3} \left(\frac{r_{\text{cloud}}}{H_{\text{disc}}} \right)^{1/3} \quad (4)$$

where $\Sigma_{\text{cloud}} \approx 10 M_{\odot} \text{ pc}^{-2}$ and is the mean surface density of the cloud, H_{disc} is the scaleheight of the disc. The level of turbulence measured in terms of $\dot{\epsilon} \propto \sigma_{v,3D}^3/r$ is proportional to $\Sigma_{\text{disc}}/\Sigma_{\text{cloud}}$, as an increased disk surface density leads to higher chances of cloud collisions. We note for this calculation to be valid, the energy injection rate should follow $\dot{\epsilon} = \sigma_{v,\text{disc}}^2 t_{\text{collisions}}$. This, we believe, is a reasonable estimate of the energy injection rate, and the results should hold whether the clouds are long-live or not. This is consistent with conclusions from simulation of barred and spiral galaxies where clouds can be relatively short lived and still collide (Fujimoto et al. 2014; Dobbs et al. 2015). We also note that results is inconsistent with the scenario of molecular cloud turbulence driven directly by stellar feedback. This is because in that case the energy injection rate should be related to $\Sigma_{\text{SF}}/\Sigma_{\text{gas}}$, where Σ_{SF} is the surface density of star formation tracers, and Σ_{gas} is the surface density of gas. To explain the varying turbulence as a function of location, we expect the star formation efficiency to vary radially, which is inconsistent

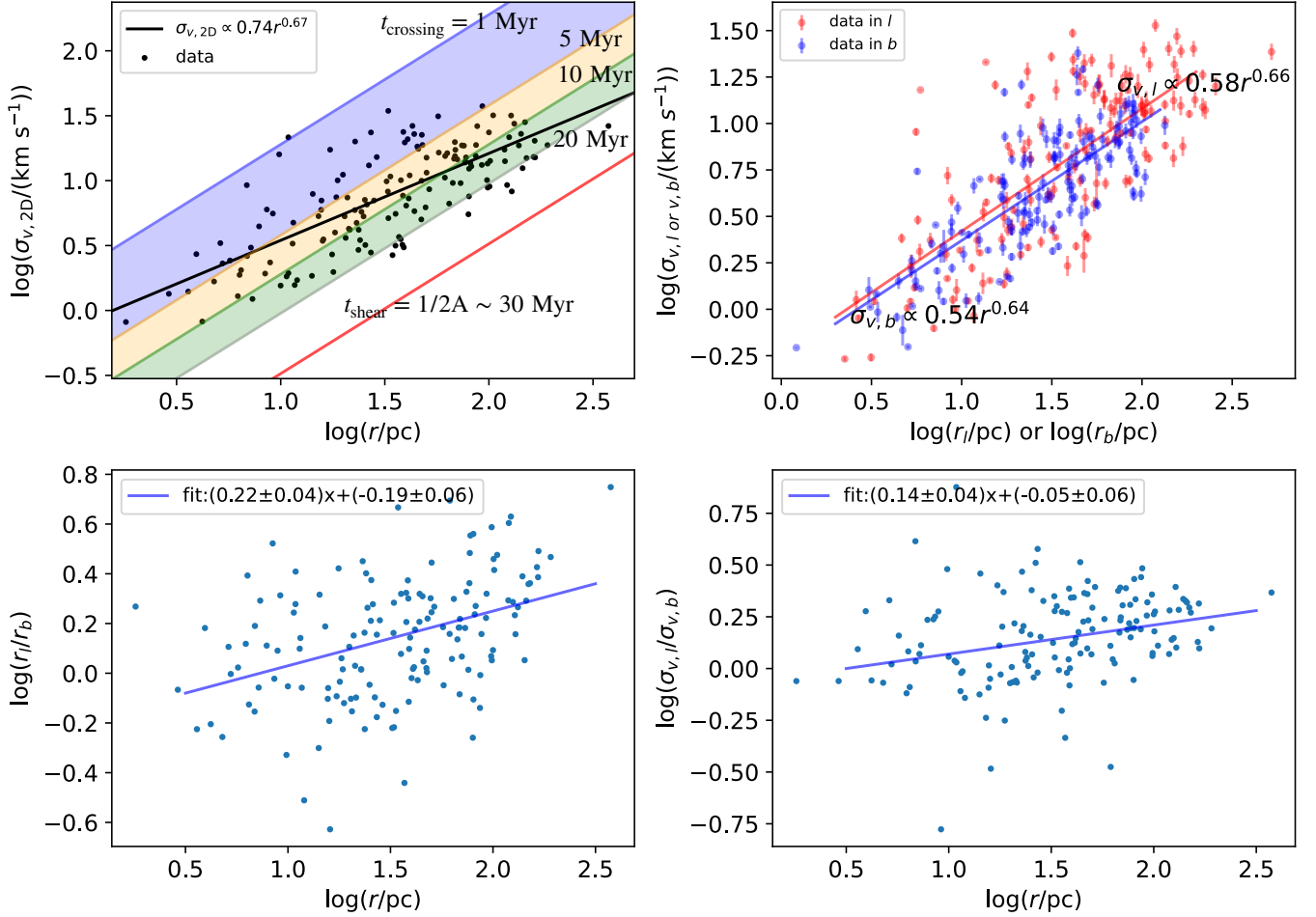


Figure 7. Relation between velocity and size. **Upper left:** $\log(\sigma_{v,2D})$ vs $\log(r)$. Black dots are the combined 2D structure data and the black line is the fitting result to the data points: $y = (0.67 \pm 0.05)x + (-0.13 \pm 0.08)$. The blue, orange, green, and grey lines refer to different crossing times. The red line is the shear time as implied by an Oort constant A of $16 \text{ km s}^{-1} \text{ kpc}^{-1}$. **Upper right:** $\log(\sigma_{v,l})$ vs $\log(r_l)$ and $\log(\sigma_{v,b})$ vs $\log(r_b)$. Red dots are the data in l direction and red line is the fitting result: $y = (0.66 \pm 0.05)x + (-0.24 \pm 0.08)$. Blue dots are the data in b direction and the blue line is the fitting result: $y = (0.64 \pm 0.04)x + (-0.27 \pm 0.06)$. **Lower left:** $\log(r_l/r_b)$ vs $\log(r)$. Blue dots are our data and the blue line is the fitting result: $y = (0.22 \pm 0.04)x + (-0.19 \pm 0.06)$. **Lower right:** $\log(\sigma_{v,l}/\sigma_{v,b})$ vs $\log(r)$. Blue dots are our data and the blue line is the fitting result: $y = (0.14 \pm 0.04)x + (-0.05 \pm 0.06)$.

with observational results which point to a constant gas depletion time (Leroy et al. 2013).

Miville-Deschênes et al. (2017) measured the surface density distribution of the Milky Way disk as a function of Galactocentric radius, and obtained the following equation:

$$\Sigma_{\text{disk}} \propto e^{-0.5 r_{\text{gal}}} \quad (5)$$

Neglecting the radial variations of H_{disk} and $\sigma_{v,\text{disk}}$, according to Eq. 4, we expect

$$\dot{\epsilon} = \eta \sigma_v^3 / l \propto e^{-0.5 r_{\text{gal}}} \quad (6)$$

which agrees with our result, where $\dot{\epsilon} \propto e^{-0.45 r_{\text{gal}}}$. The decreasing energy dissipation rate of the molecular cloud turbulence with increasing r_{gal} is likely caused by the decrease of surface density of the molecular disc, which leads to a lower collisional rate. We note that in our picture, we focus on the change of the cloud-averaged energy dissipation rate. Small(sub-kpc)-scale fluctuations of surface density might lead to local variations in the energy dissipation, which is averaged out after we have divided our clouds into groups.

5 CONCLUSIONS

Using a sample of 15149 YSOs younger than 3 Myr, we extract 150 associations with sizes ranging from several pc to one hundred pc and study their velocity structures. This allows us to probe the velocities of the gas that these YSOs are associated with. Our major results include:

- (i) All the structures are elongated and are orientated parallel to the Galactic mid-plane.
- (ii) We find that the velocity dispersions and sizes are related by $\sigma_{v,2D} = 0.74 (r/\text{pc})^{0.67 \pm 0.05} (\text{km s}^{-1})$, which is often called the Larson relation. The exponent 0.67 is consistent with recent simulation results.
- (iii) Using proper motion measurements, we study the velocity dispersion-size relation measured along the Galactic longitude and latitude separately. Along l direction, we obtain $\sigma_{v,l} = 0.58 (r_l/\text{pc})^{0.66} (\text{km s}^{-1})$ and along b direction, we obtain $\sigma_{v,b} = 0.54 (r_b/\text{pc})^{0.64} (\text{km s}^{-1})$. The results indicate that turbulence in molecular clouds is isotropic.

(iv) Although the density structure is anisotropic, the turbulence is consistent with being isotropic. This can be explained if molecular clouds are long-lived ($t_{\text{cloud}} \gtrsim t_{\text{shear}}$), such that their overall density structures are shaped by Galactic-scale process such as shear. During the cloud lifetime, turbulence is maintained by a continuous injection.

(v) We compute the energy dissipation rate of turbulence using $\sigma_{v,3D}^3/r$, and find it depends on the distance from the Galactic center r_{gal} , where $\dot{\epsilon} = 1.77 \times 10^{-4} e^{-0.45(r_{\text{gal}}/(\text{pc}))} (\text{erg g}^{-1} \text{ s}^{-1})$, where a slope of 0.20 dex kpc^{-1} is implied.

(vi) The decreasing energy dissipation rate with increasing Galactocentric radius can be explained by a reduction of clouds collisions rates, as the clouds located in the inner Galaxy where the disk surface densities are higher have higher changes of accreting smaller clouds.

ACKNOWLEDGEMENTS

We thank our referees whose comments helped to improve our paper significantly. This work is partially supported by the Postgraduate's Research and Innovation Project of Yunnan University (No. 2019236). GXL acknowledges supports from NSFC grant W820301904 and 12033005. BQC is supported by the National Key R&D Program of China No. 2019YFA0405500, National Natural Science Foundation of China 12173034, 11803029 and 11833006, and the science research grants from the China Manned Space Project with NO. CMS-CSST-2021-A09, CMS-CSST-2021-A08 and CMS-CSST-2021-B03.

This work presents results from the European Space Agency (ESA) space mission Gaia. Gaia data are being processed by the Gaia Data Processing and Analysis Consortium (DPAC). Funding for the DPAC is provided by national institutions, in particular the institutions participating in the Gaia MultiLateral Agreement (MLA). The Gaia mission website is <https://www.cosmos.esa.int/gaia>. The Gaia archive website is <https://archives.esac.esa.int/gaia>. This research has used ASTRODENDRO, a PYTHON package to compute dendrograms of Astronomical data (<http://www.dendrograms.org/>).

DATA AVAILABILITY

The paper makes use of published data from [Marton et al. \(2016\)](#) and Gaia DR2 ([Gaia Collaboration et al. 2018](#)). Our Table A1 will be made available online upon publication.

REFERENCES

Abreu-Vicente J., Ragan S., Kainulainen J., Henning T., Beuther H., Johnston K., 2016, *A&A*, **590**, A131
 Alves J., et al., 2020, *Nature*, **578**, 237
 Ballesteros-Paredes J., Hartmann L. W., Vázquez-Semadeni E., Heitsch F., Zamora-Avilés M. A., 2011, *MNRAS*, **411**, 65
 Bolatto A. D., Leroy A. K., Rosolowsky E., Walter F., Blitz L., 2008, *ApJ*, **686**, 948
 Cen R., 2021, *ApJ*, **906**, L4
 Chen B. Q., et al., 2019a, *MNRAS*, **483**, 4277
 Chen B. Q., et al., 2019b, *MNRAS*, **487**, 1400
 Chen B. Q., et al., 2020, *MNRAS*, **493**, 351
 Cutri R. M., et al., 2003, 2MASS All Sky Catalog of point sources.
 Cutri R. M., et al., 2021, VizieR Online Data Catalog, **p. II/328**
 Dobbs C. L., Burkert A., Pringle J. E., 2011, *MNRAS*, **413**, 2935
 Dobbs C. L., Pringle J. E., Duarte-Cabral A., 2015, *MNRAS*, **446**, 3608
 Dunham M. M., et al., 2015, *ApJS*, **220**, 11
 Elmegreen B. G., Burkert A., 2010, *ApJ*, **712**, 294

Frisch U., 1995, Turbulence. The legacy of A.N. Kolmogorov
 Fujimoto Y., Tasker E. J., Wakayama M., Habe A., 2014, *MNRAS*, **439**, 936
 Gaia Collaboration et al., 2016, *A&A*, **595**, A1
 Gaia Collaboration et al., 2018, *A&A*, **616**, A1
 Goldbaum N. J., Krumholz M. R., Forbes J. C., 2015, *ApJ*, **814**, 131
 Goodman A. A., et al., 2014, *ApJ*, **797**, 53
 Großschedl J. E., Alves J., Meingast S., Herbst-Kiss G., 2021, *A&A*, **647**, A91
 Ha T., Li Y., Xu S., Kounkel M., Li H., 2021, *ApJ*, **907**, L40
 Hennebelle P., Chabrier G., 2008, *ApJ*, **684**, 395
 Heyer M., Krawczyk C., Duval J., Jackson J. M., 2009, *ApJ*, **699**, 1092
 Hopkins P. F., 2013, *MNRAS*, **430**, 1653
 Hughes A., et al., 2013, *ApJ*, **779**, 46
 Ibáñez-Mejía J. C., Mac Low M.-M., Klessen R. S., Baczynski C., 2016a, *ApJ*, **824**, 41
 Ibáñez-Mejía J. C., Mac Low M.-M., Klessen R. S., Baczynski C., 2016b, *ApJ*, **824**, 41
 Izquierdo A. F., et al., 2021, *MNRAS*, **500**, 5268
 Jackson J. M., et al., 2006, *ApJS*, **163**, 145
 Kauffmann J., Pillai T., Zhang Q., Menten K. M., Goldsmith P. F., Lu X., Guzmán A. E., 2017, *A&A*, **603**, A89
 Kerr F. J., Lynden-Bell D., 1986, *MNRAS*, **221**, 1023
 Klessen R. S., Hennebelle P., 2010, *A&A*, **520**, A17
 Koda J., 2021, *Research Notes of the American Astronomical Society*, **5**, 222
 Koda J., Sawada T., Hasegawa T., Scoville N. Z., 2006, *ApJ*, **638**, 191
 Kolmogorov A. N., 1941, Doklady Akademii Nauk Sssr, **31**
 Kritsuk A. G., Lee C. T., Norman M. L., 2013, *MNRAS*, **436**, 3247
 Kruijssen J. M. D., et al., 2019, *Nature*, **569**, 519
 Larson R. B., 1981, *MNRAS*, **194**, 809
 Leroy A. K., et al., 2013, *AJ*, **146**, 19
 Li G.-X., 2017, *MNRAS*, **471**, 2002
 Li G.-X., Wyrowski F., Menten K., Belloche A., 2013, *A&A*, **559**, A34
 Li H. B., Goodman A., Sridharan T. K., Houde M., Li Z. Y., Novak G., Tang K. S., 2014, in Beuther H., Klessen R. S., Dullemond C. P., Henning T., eds, Protostars and Planets VI. p. 101 ([arXiv:1404.2024](https://arxiv.org/abs/1404.2024)), [doi:10.2458/azu_uapress_9780816531240-ch005](https://doi.org/10.2458/azu_uapress_9780816531240-ch005)
 Li G.-X., Urquhart J. S., Leurini S., Csengeri T., Wyrowski F., Menten K. M., Schuller F., 2016, *A&A*, **591**, A5
 Lim W., et al., 2021, *PASJ*, **73**, S239
 Liu L., Bureau M., Blitz L., Davis T. A., Onishi K., Smith M., North E., Iguchi S., 2021, *MNRAS*, **505**, 4048
 Mac Low M.-M., 1999, *ApJ*, **524**, 169
 Mac Low M. M., 2003, MHD Turbulence in Star-Forming Regions and the Interstellar Medium. pp 182–212
 Marton G., Tóth L. V., Paladini R., Kun M., Zahorecz S., McGehee P., Kiss C., 2016, *MNRAS*, **458**, 3479
 Meidt S. E., et al., 2015, *ApJ*, **806**, 72
 Miville-Deschênes M.-A., Murray N., Lee E. J., 2017, *ApJ*, **834**, 57
 Oort J. H., 1927, Bull. Astron. Inst. Netherlands, **3**, 275
 Padoan P., Nordlund Å., 2002, *ApJ*, **576**, 870
 Planck Collaboration et al., 2014, *A&A*, **571**, A16
 Qian L., Li D., Gao Y., Xu H., Pan Z., 2018, *ApJ*, **864**, 116
 Ragan S. E., Henning T., Tackenberg J., Beuther H., Johnston K. G., Kainulainen J., Linz H., 2014, *A&A*, **568**, A73
 Roman-Duval J., Jackson J. M., Heyer M., Rathborne J., Simon R., 2010, *ApJ*, **723**, 492
 Rosolowsky E. W., Pineda J. E., Kauffmann J., Goodman A. A., 2008, The Astrophysical Journal, **679**
 Schuller F., et al., 2009, *A&A*, **504**, 415
 Shetty R., Beaumont C. N., Burton M. G., Kelly B. C., Klessen R. S., 2012, *MNRAS*, **425**, 720
 Solomon P. M., Rivolo A. R., Barrett J., Yahil A., 1987, *ApJ*, **319**, 730
 Sun J., et al., 2018, *ApJ*, **860**, 172
 Vázquez-Semadeni E., González-Samaniego A., Colín P., 2017, *MNRAS*, **467**, 1313
 Wang K., Testi L., Ginsburg A., Walmsley C. M., Molinari S., Schisano E., 2015, *MNRAS*, **450**, 4043

Wang F., Zhang H. W., Huang Y., Chen B. Q., Wang H. F., Wang C., 2021,
[MNRAS, 504, 199](#)

APPENDIX A: PARAMETERS OF ASSOCIATIONS

In Table.A1, we list the properties of the associations, including the mean longitude, the mean latitude, the number of the member stars, the mean distance, the position angle, and aspect ratio in $l-b$ and v_l-v_b space, the angle difference between $l-b$ and v_l-v_b space, the velocity dispersion in l and b directions, the combined 2D velocity dispersion, the size in l and b directions, and the combined size of some of the 150 associations.

Table A1: Parameters of YSO associations (only a fraction of the table is shown and the full table can be downloaded online http://paperdata.china-vo.org/zjx/ysso_association/upload_association_para.csv).

id	$l(^{\circ})$	$b(^{\circ})$	n_{star}	d (kpc)	$PA_{v_l-v_b}(^{\circ})$	$A_{v_l-v_b}$	$PA_{l-b}(^{\circ})$	A_{l-b}	$\Delta A(^{\circ})$	σ_{v_l} (km/s)	σ_{v_b} (km/s)	$\sigma_{v,2D}$ (km/s)	r_l (pc)	r_b (pc)	r (pc)
G171.700-015.500	171.67	-15.461	62	0.13	-41.33	1.7	10.25	2.89	51.57	1.43	1.33	1.61	14.36	5.6	10.9
G169.600-015.700	169.56	-15.704	33	0.13	-33.19	1.62	11.71	2.87	44.9	1.46	1.21	1.6	8.32	3.37	6.35
G168.700-015.900	168.681	-15.883	24	0.13	-64.2	1.3	-84.77	1.17	20.57	0.9	1.03	0.99	2.67	3.12	2.9
G174.500-015.000	174.466	-14.997	45	0.14	57.49	1.79	-63.54	1.66	58.96	1.31	1.61	1.13	5.47	7.3	6.45
G338.200+009.000	338.205	8.989	47	0.16	-25.54	2.96	14.48	6.49	40.03	1.67	0.96	0.92	11.4	3.43	8.42
G336.422+008.600	336.422	8.562	21	0.16	-25.4	4.07	28.86	2.59	54.26	2.41	1.27	1.23	4.65	3.06	3.94
G339.665+009.300	339.665	9.346	24	0.16	-71.61	1.22	3.45	1.87	75.06	0.54	0.62	0.53	2.25	1.21	1.81
G352.880+019.500	352.88	19.484	255	0.14	-76.84	1.43	-84.38	2.04	7.54	1.12	1.5	1.13	8.94	17.87	14.13
G353.255+018.900	353.255	18.906	166	0.14	-76.76	1.49	86.0	3.33	17.24	1.01	1.41	1.03	5.0	16.21	11.99
G353.199+017.000	353.199	17.012	107	0.14	-76.26	1.23	82.05	1.86	21.68	1.1	1.29	1.14	3.28	5.92	4.79
G353.383+022.500	353.383	22.473	68	0.14	-84.42	1.36	24.8	1.55	70.78	0.79	1.04	0.81	7.0	5.33	6.23
G297.100-015.200	297.064	-15.248	59	0.19	-15.3	1.27	-71.88	1.97	56.58	1.12	0.91	1.07	2.6	4.37	3.6
G303.600-014.700	303.583	-14.666	24	0.2	54.32	1.71	70.31	1.91	15.98	0.55	0.63	0.64	3.14	5.04	4.2
G158.400-020.700	158.446	-20.742	49	0.3	-12.48	1.47	41.79	1.67	54.27	2.05	1.42	2.03	5.86	5.55	5.71
G160.300-017.900	160.342	-17.938	33	0.32	12.45	2.42	24.01	1.46	11.56	3.02	1.41	2.37	5.71	4.47	5.13
G104.424+014.000	104.424	14.017	18	0.33	10.7	1.36	-21.06	2.92	31.76	1.0	0.77	0.81	9.22	4.71	7.32
G208.400-018.400	208.356	-18.439	525	0.39	43.87	1.11	-34.06	1.98	77.94	2.18	2.18	1.96	43.11	34.42	39.01
G210.100-019.500	210.082	-19.484	285	0.39	-8.2	1.31	0.16	2.64	8.36	2.15	1.66	1.77	23.35	8.84	17.66
G206.000-016.300	205.964	-16.34	155	0.4	60.32	1.36	-68.98	1.64	50.7	2.38	2.77	2.28	16.68	23.74	20.52
G206.400-017.000	206.432	-16.955	79	0.4	61.76	1.62	13.14	1.29	48.62	2.01	2.59	2.09	12.62	10.05	11.41
G345.218+000.800	345.218	0.778	89	1.59	-36.42	1.82	-19.67	2.71	16.75	13.29	11.31	14.17	149.76	76.25	118.83
G344.161+001.200	344.161	1.222	60	1.57	-41.15	2.44	-31.19	1.34	9.96	12.12	10.94	13.4	67.09	58.77	63.07
G352.350+002.800	352.35	2.8	42	1.07	-14.24	3.12	15.38	1.66	29.61	18.38	7.47	15.2	81.2	53.16	68.63
G335.700-001.500	335.746	-1.516	29	1.18	-18.6	1.57	-13.47	4.44	5.12	11.4	8.05	9.85	103.57	34.02	77.09
G333.948+000.300	333.948	0.304	45	2.14	9.22	2.69	-11.5	1.81	20.72	29.47	11.89	29.64	156.06	91.16	127.8
G336.700-001.800	336.745	-1.756	24	1.17	51.3	1.58	8.57	1.97	42.73	4.41	4.87	5.52	32.45	17.13	25.95
G333.892+000.200	333.892	0.196	33	2.22	6.82	1.96	-10.0	1.94	16.83	24.49	12.75	24.12	164.54	89.27	132.37
G304.110+000.600	304.11	0.554	80	2.12	-2.5	1.96	-12.91	2.67	10.4	25.21	12.79	25.12	193.07	84.52	149.03
G307.000-000.000	307.05	-0.011	15	2.17	-74.32	1.21	-14.62	1.65	59.7	20.44	23.93	22.11	67.57	44.08	57.04
G303.056+000.800	303.056	0.804	45	1.97	1.84	3.09	3.25	1.44	1.42	24.95	8.18	24.99	102.03	70.97	87.88
G303.191+001.100	303.191	1.128	29	1.83	16.21	1.69	1.25	3.59	14.96	12.92	8.24	12.95	105.7	29.52	77.6
G302.240+001.100	302.24	1.139	18	1.82	15.23	1.84	12.35	2.27	2.88	16.0	9.5	15.72	57.55	28.22	45.32
G294.900-001.400	294.916	-1.392	34	2.42	13.43	1.81	-78.52	1.24	88.05	13.61	7.96	13.38	61.76	75.06	68.73
G290.577+000.400	290.577	0.422	62	2.44	-4.39	1.53	-77.95	1.43	73.55	13.2	8.53	13.22	71.74	98.9	86.39
G290.600-000.100	290.555	-0.118	39	2.5	-3.26	1.47	-17.88	1.71	14.62	12.43	8.33	12.59	80.48	52.72	68.03
G283.200-001.900	283.201	-1.877	38	2.53	14.37	3.78	51.64	1.08	37.27	18.01	6.52	18.14	85.97	87.49	86.74
G286.900-000.700	286.906	-0.666	27	2.63	-20.02	1.78	-13.04	2.43	6.98	15.91	10.33	14.88	95.0	44.67	74.23
G086.975+003.900	86.975	3.932	16	1.62	18.88	1.7	47.99	2.06	29.11	22.07	14.7	18.08	41.54	44.31	42.94
G068.600-001.200	68.587	-1.207	18	1.87	7.89	1.14	2.81	3.94	5.08	10.3	8.95	10.29	134.89	34.88	98.52